Pyroelectric waste heat energy harvesting using relaxor ferroelectric 8/65/35 PLZT and the Olsen cycle

2012 Smart Mater. Struct. 21 025021

(http://iopscience.iop.org/0964-1726/21/2/025021)

Smart Mater. Struct. **21** (2012) 025021 (12pp) doi:10.1088/0964-1726/21/2/025021

Pyroelectric waste heat energy harvesting using relaxor ferroelectric 8/65/35 PLZT and the Olsen cycle

Felix Y Lee, Sam Goljahi, Ian M McKinley, Christopher S Lynch and Laurent Pilon[1]

Mechanical and Aerospace Engineering Department, Henry Samueli School of Engineering and Applied Science, University of California, Los Angeles, Los Angeles, CA 90095, USA

E-mail: pilon@seas.ucla.edu

Received 20 October 2011, in final form 9 December 2011
Published 26 January 2012
Online at stacks.iop.org/SMS/21/025021

Abstract
Waste heat can be directly converted into electrical energy by performing the Olsen cycle on pyroelectric materials. The Olsen cycle consists of two isothermal and two isoelectric field processes in the electric displacement versus electric field diagram. This paper reports on the electrical energy generated by lanthanum-doped lead zirconate titanate (8/65/35 PLZT) subjected to the Olsen cycle. The material was alternately dipped into a cold and a hot silicone oil bath under specified electric fields. A maximum energy density of 888 J l^{-1}/cycle was obtained with a 290 μm thick 8/65/35 PLZT sample for temperatures between 25 and 160 °C and electric fields cycled between 0.2 and 7.5 MV m^{-1}. To the best of our knowledge, this is the largest pyroelectric energy density experimentally measured with multiple cycles. It corresponded to a power density of 15.8 W l^{-1}. The electrical breakdown strength and therefore the energy and power densities of the material increased as the sample thickness was reduced from 720 to 290 μm. Furthermore, a physical model for estimating the energy harvested by ferroelectric relaxors was further validated against experimental data for a wide range of electric fields and temperatures.

(Some figures may appear in colour only in the online journal)

1. Introduction

Waste heat is rejected as a by-product of power, refrigeration or heat pump cycles as a consequence of the second law of thermodynamics. In 2009, more than 55% of the energy consumed in the United States was lost as low temperature waste heat [1]. For example, the transportation sector contributed to 37% of the total waste heat. This is due to the fact that about 25–35% of the energy contained in the fuel of cars and trucks is typically converted into useful energy while the rest is dissipated as heat through the radiator and the exhaust pipe [2]. In the past decade, direct energy conversion technologies for harvesting low temperature waste heat have received significant attention. For example, thermoelectric devices directly convert a steady-state temperature difference at the junction of two dissimilar materials into electrical energy based on the Seebeck effect [3]. Alternatively, the pyroelectric effect consists of directly converting a time-dependent temperature oscillation into electrical energy [4–21]. In practice, the generated energy can be harvested by delivering it to an external load or storage unit [22]. Several pyroelectric devices have been designed and operated to create the temporal temperature oscillations required in pyroelectric waste heat harvesting [4–12, 15–18, 21–28]. The required temperature oscillations have been achieved passively in various designs [27, 28]. In order to achieve the maximum device performance, it is also necessary to identify the pyroelectric material that generates the largest amount of energy and power densities for a given temperature range.

[1] www.seas.ucla.edu/~pilon.

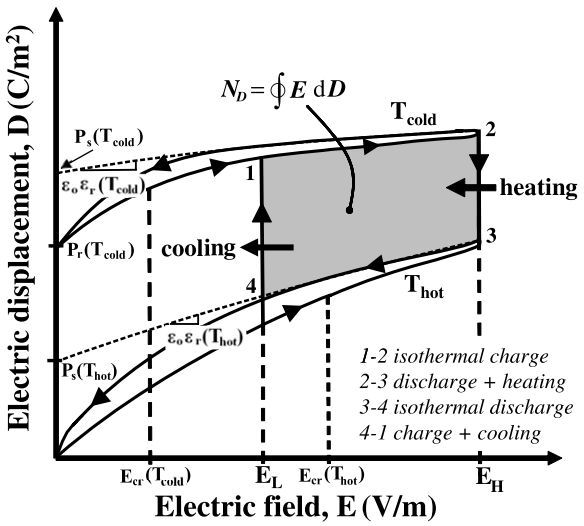

Figure 1. Isothermal unipolar electric displacement versus electric field (*D–E*) hysteresis loops for a typical pyroelectric material at temperatures T_{hot} and T_{cold} along with the Olsen cycle. The electrical energy generated per cycle is represented by the area enclosed between 1–2–3–4.

This paper reports, for the first time, experimental measurements of the energy harvested by commercially available lead lanthanum zirconate titanate (PLZT) subjected to the Olsen cycle. The effects of low electric field E_L, cold source temperature T_{cold}, hot source temperature T_{hot} and high electric field E_H on the energy harvested were systematically investigated. Then, experimental data were compared with predictions made by a recently developed physical model [19].

2. Background

2.1. Pyroelectricity/ferroelectricity

Pyroelectric materials possess a spontaneous polarization defined as the average electric dipole moment per unit volume in the absence of an applied electric field [29]. A subclass of pyroelectric materials known as ferroelectric materials have the ability to switch the direction and magnitude of the spontaneous polarization by reversing the applied coercive electric field [30].

Figure 1 shows the isothermal unipolar hysteresis curves between electric displacement D and electric field E exhibited by a pyroelectric material at two different temperatures T_{cold} and T_{hot}. These so-called *D–E* loops are traveled in a counter-clockwise direction. The *D–E* loops corresponding to T_{cold} and T_{hot} are characteristic of a typical ferroelectric and paraelectric material, respectively. In fact, a ferroelectric material undergoes a phase transition from ferroelectric to paraelectric when it is heated above its Curie temperature, denoted by T_{Curie}. Then, the spontaneous polarization vanishes. The electric displacement D of an isotropic material at electric field E and temperature T can be expressed as [30, 31]

$$D(E, T) = \varepsilon_0\varepsilon_r(T)E + P_s(T) \quad (1)$$

where ε_o is the vacuum permittivity ($=8.854\times10^{12}$ F m^{-1}) and $\varepsilon_r(T)$ is the relative permittivity of the material at electric field E and temperature T. The saturation polarization denoted by $P_s(T)$ is estimated as the displacement in the linear fit of D versus E extrapolated at zero electric field. The slope of this linear fit corresponds to the product $\varepsilon_0\varepsilon_r(T)$ as illustrated in figure 1.

2.2. Olsen cycle

The Olsen cycle consists of two isothermal and two isoelectric processes in the electric displacement versus electric field (*D–E*) diagram [7] as illustrated in figure 1. Process 1–2 consists of charging the pyroelectric element (PE) at T_{cold} by increasing the applied electric field from E_L to E_H. Process 2–3 corresponds to discharging the PE by heating it from T_{cold} to T_{hot} under constant electric field E_H. Process 3–4 consists of reducing the electric field from E_H to E_L under isothermal conditions at T_{hot}. Finally, process 4–1 closes the cycle by cooling the PE from T_{hot} to T_{cold} under constant electric field E_L. Note that the Olsen cycle, in the *D–E* diagram, is analogous to the Ericsson cycle defined in the pressure versus specific volume diagram.

The area enclosed by the clockwise 1–2–3–4 loop in the *D–E* curve represents the electric energy produced per unit volume of material per cycle denoted by N_D (in J l^{-1}/cycle) and defined as [7]

$$N_D = \oint E\,dD. \quad (2)$$

The corresponding power density P_D (in W l^{-1}) produced by the pyroelectric element is expressed as

$$P_D = N_D f \quad (3)$$

where f is the cycle frequency. Note that N_D is also dependent on the cycle frequency [18, 20].

2.3. Materials

Relaxor ferroelectrics are a promising class of materials which feature exceptional electro-optical, dielectric and piezoelectric properties [32]. These materials can be used in devices such as piezoelectric actuators, pyroelectric sensors, multilayer capacitors and optical shutters [33]. The material investigated in this study is a relaxor ferroelectric composed of 8 mol% lanthanum doped into a 65 mol% lead zirconate and 35 mol% lead titanate solid solution ($Pb_{0.92}La_{0.08}(Zr_{0.65}Ti_{0.35})_{0.98}O_3$), also denoted as 8/65/35 PLZT [34]. The lanthanum doping increases the resistivity of the material and contributes to the strong electromechanical coupling [34–36]. At room temperature, the 8/65/35 PLZT crystal structure has rhombohedral symmetry [37]. The material undergoes complex phase transitions which are very sensitive to temperature and applied electric field [35]. It is paraelectric beyond the Burns temperature $T_B \simeq 350\,^{\circ}$C [38]. Upon cooling below T_B, the material transforms from the paraelectric phase to the ergodic relaxor phase. In the latter phase, nanoscale polar regions with randomly distributed

dipoles form and give rise to large dielectric and piezoelectric properties [39].

The phase transition between ergodic relaxor and ferroelectric is field-dependent and occurs at the Curie temperature T_{Curie}. The latter can be determined from the maximum of the pyroelectric current $(\partial D/\partial T)_{\sigma,E}$ versus temperature T curve measured under a specified electric field E. The material can revert phase from ferroelectric to ergodic relaxor by heating it above T_{Curie} and/or depoling below a critical electric field $E_{\text{cr}}(T)$. The Curie temperature T_{Curie} is expected to become nearly frequency-independent in the vicinity of the ergodic-relaxor–ferroelectric phase transition [40]. This is due to the reduction in dipole thermal fluctuations as the material is cooled below T_{Curie} [40–42]. In 8/65/35 PLZT, the ferroelectric phase cannot be established upon cooling under zero electric field [43]. However, the ferroelectric phase can be induced from the ergodic relaxor phase by applying an external electric field E greater than $E_{\text{cr}}(T)$ [44–47]. Unfortunately, T_{Curie} and $E_{\text{cr}}(T)$ for the PLZT composition 8/65/35 have not been reported in the literature. Therefore, we can only speculate upon the ferroelectric–relaxor phase transitions in 8/65/35 PLZT based on data reported for 9/65/35 PLZT [47, 48].

Note also that the remnant polarization $P_{\text{r}}(T)$ of ferroelectric relaxors does not vanish above T_{Curie} due to the persistence of nanopolar domains interacting with each other at temperatures between T_{Curie} and T_{B} [42]. However, the remnant polarization is negligibly small in the relaxor state with respect to its value in the ferroelectric state [42].

The converse of the pyroelectric effect is the electrocaloric effect. It is the change in temperature caused by a change in applied electric field under adiabatic conditions [49]. Lu *et al* [50] recently demonstrated a large electrocaloric effect on 8/65/35 PLZT thin films. The electrocaloric temperature change of $\Delta T = 40$ K was observed for 0.45 μm thick 8/65/35 PLZT at about 45 °C under an electric field of 125 MV m^{-1}. In addition, Sebald *et al* [51] have shown theoretically that materials exhibiting large electrocaloric activity are of interest in pyroelectric energy harvesting. Consequently, the present study aims to experimentally assess the pyroelectric energy harvesting capabilities of 8/65/35 PLZT.

2.4. Physical modeling of the Olsen cycle

Recently, Kandilian *et al* [19] developed a physical model predicting the amount of energy harvested by relaxor ferroelectric materials undergoing the Olsen cycle. The model accounted for temperature-dependent properties of the material. The energy density N_{D} was expressed as [19]

$$N_{\text{D}}(E_{\text{L}}, E_{\text{H}}, T_{\text{cold}}, T_{\text{hot}}) = (E_{\text{H}} - E_{\text{L}}) \times \left\{ \frac{\varepsilon_0}{2}[\varepsilon_{\text{r}}(T_{\text{cold}}) - \varepsilon_{\text{r}}(T_{\text{hot}})](E_{\text{H}} + E_{\text{L}}) + P_{\text{s}}(T_{\text{cold}}) - P_{\text{s}}(T_{\text{hot}}) + \frac{d_{33}x_3}{s_{33}} \right\} \quad (4)$$

where $\varepsilon_{\text{r}}(T_{\text{cold}})$ and $\varepsilon_{\text{r}}(T_{\text{hot}})$ are the low frequency relative permittivities of the pyroelectric material at the cold and hot operating temperatures T_{cold} and T_{hot}, respectively. The saturation polarizations of the material at T_{cold} and T_{hot} are denoted by $P_{\text{s}}(T_{\text{cold}})$ and $P_{\text{s}}(T_{\text{hot}})$, respectively, and expressed in C m^{-2}. Note that Kandilian *et al* [19] erroneously called $P_{\text{s}}(T)$ the spontaneous polarization instead of saturation polarization, as sometimes found in the literature [52]. The piezoelectric coefficient d_{33} is expressed in C N^{-1}, s_{33} is the elastic compliance (in m^2 N^{-1}) and $x_3 = \alpha_3(T_{\text{hot}} - T_{\text{cold}})$, where α_3 is the linear thermal expansion coefficient (in K^{-1}). Note that this model was based on the assumption that the dielectric contribution to the primary pyroelectric coefficient was negligible compared with the dipole contribution (see equation (8) in [19]). The model successfully predicted the energy density harvested by PMN-32PT [19] and PZN-5.5PT [20]. Here also, the model predictions will be compared with the energy density experimentally measured with 8/65/35 PLZT.

Table 1. Thickness and cross-sectional area of the different 8/65/35 PLZT samples and their electrodes investigated in this study.

Sample #	Thickness (μm)	Electrode size (cm × cm)	Sample size (cm × cm)
1	490	0.81 × 0.90	0.81 × 0.90
2	720	0.815 × 0.95	0.815 × 0.95
3	600	0.90 × 0.95	0.90 × 0.95
4	650	0.979 × 0.838	0.979 × 0.838
5	370	0.845 × 0.653	0.991 × 0.843
6	370	0.833 × 0.644	0.993 × 0.839
7	290	0.414 × 0.429	0.876 × 0.852

3. Experiments

3.1. Samples

Hot isostatically pressed 8/65/35 PLZT ceramics with grain diameter around 5 μm were acquired from Aura Ceramics, Inc. (New Hope, MN, USA). The specimen was cut into seven samples with thicknesses ranging from 290 to 720 μm using a diamond abrasive saw. Rectangular gold electrodes were sputtered on opposite faces. Electrical wires were bonded to the electrodes using conductive silver epoxy. Table 1 lists the thickness and the cross-sectional dimensions of each sample used in this study. Note that the electrodes in samples 5–7 did not fully cover the faces. This electrode configuration was chosen in order to minimize electrical conduction (leakage current) around the samples' edges.

3.2. Experimental set-up

Two thermally insulated beakers containing Dow Corning 100 cSt silicone oil were maintained at temperatures T_{cold} and T_{hot} thanks to temperature-controlled hot plates [19, 23]. J-type thermocouples were immersed in each bath to monitor and control their temperature. The samples were alternately dipped between the cold and hot baths to create the temporal temperature oscillations required in the Olsen cycle. Sufficient time (∼20–60 s) was given for the sample's

electric displacement to reach steady state ($\partial D/\partial t = 0$) during processes 2–3 and 4–1 before varying the electric field and then moving the sample from one bath to the other. This ensures that the cycle was performed under quasiequilibrium conditions to achieve the maximum energy density. Note that the thermal characteristic time constant can be estimated as $\tau = \rho c_p/hb$ [53], where h is the heat transfer coefficient and b is the sample thickness, while ρ and c_p are the sample density and specific heat, respectively. For example, the thermal characteristic time constant was estimated to be 2.5 s for a 290 μm thick 8/65/35 PLZT sample with $\rho =$ 7900 kg m^{-3} [54], $c_p = 329$ J kg^{-1} K^{-1} [55] and $h =$ 300 W m^{-2} K^{-1}, corresponding to convective quenching in an oil bath [56].

The electrical subsystem used to perform the Olsen cycle consisted of a modified Sawyer–Tower circuit [31] to apply the required electric field across the pyroelectric material and to measure the charge Q collected at the electrode surfaces. Details of the circuit used in the present study were provided in [19] and need not be repeated. This circuit was also used to measure the unipolar and bipolar D–E loops at various temperatures.

3.3. Experimental procedure

3.3.1. Isothermal D–E loops. Isothermal unipolar and bipolar D–E loops were collected at 45, 65, 100, 110, 120, 130 and 160 °C for samples 4–6 and at 25 and 160 °C for sample 7 using the electrical circuit previously discussed. The measurements were taken while the sample was immersed in a silicone oil bath maintained at the desired temperature. For bipolar loop measurements, a continuous triangular voltage signal was applied across the sample at 0.33 Hz, corresponding to the frequency at which the electric field was changed during isothermal processes 1–2 and 3–4 in the Olsen cycle. The amplitude of the applied voltage corresponded to an electric field cycled between −2.5 and 2.5 MV m^{-1}. Similarly, the applied voltage for unipolar D–E loop measurements corresponded to an electric field varying from 0.0 to 2.5 MV m^{-1}. These measurements were taken at 0.66 Hz, corresponding to the same rate of change in electric field as that imposed to collect the 0.33 Hz bipolar D–E loops.

Moreover, the saturation polarization $P_s(T)$, the remnant polarization $P_r(T)$ and the relative permittivity $\varepsilon_r(T)$ of 8/65/35 PLZT samples were evaluated by linearly fitting the upper curve of isothermal bipolar D–E loops corresponding to a decrease in electric field from E_H to E_L as shown in figure 1.

3.3.2. Olsen cycle. The Olsen cycle was performed on 8/65/35 PLZT at various electric fields and temperatures to investigate their respective effects on the energy harvested. For example, the low electric field E_L was varied between 0.0 and 0.4 MV m^{-1} and the high electric field E_H from 0.4 to 7.5 MV m^{-1}. The cold source temperature T_{cold} was either 25, 45 or 65 °C, while the hot source temperature was varied from 100 to 160 °C. The Olsen cycles were recorded in the D–E diagram and the energy density N_D, defined in equation (2), was estimated by applying the trapezoidal rule.

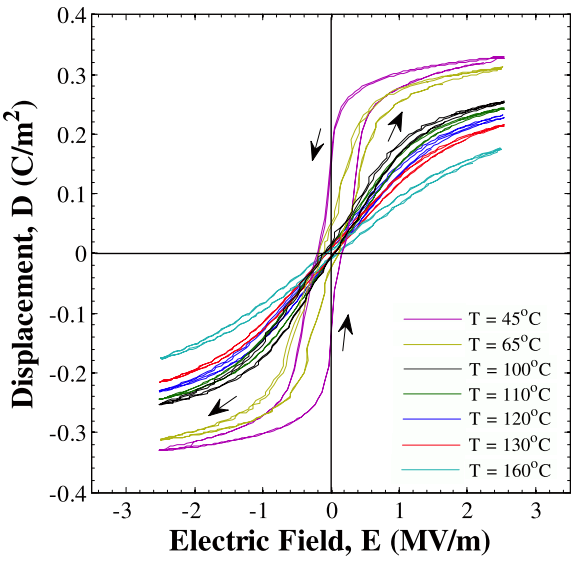

Figure 2. Bipolar isothermal electric displacement versus electric field (D–E) hysteresis curves at various temperatures (colored figure). The D–E paths travel in a counter-clockwise direction. The electric field was cycled between −2.5 and 2.5 MV m^{-1} at 0.33 Hz. The D–E loops at 45 and 65 °C correspond to the ferroelectric phase while those at 100, 110, 120, 130 and 160 °C indicate that the material was in the ergodic relaxor phase.

4. Experimental results and discussion

4.1. D–E loops

Figure 2 plots the bipolar D–E loops at 45, 65, 100, 110, 120, 130 and 160 °C measured at 0.33 Hz with sample 4. The electric field was isothermally cycled between −2.5 and 2.5 MV m^{-1}. The isothermal D–E loops corresponding to 45 and 65 °C featured square loops typical of a ferroelectric state. On the other hand, the D–E loops corresponding to 100, 110, 120, 130 and 160 °C exhibited slim linear hysteresis with small remnant polarization ($P_r \leq 0.02$ C m^{-2}), indicating that the material was in the ergodic relaxor phase. Note that the unipolar D–E loops (not shown) were very narrow with little hysteresis and nearly identical to the upper curve of the bipolar D–E loops between 0 and 2.5 MV m^{-1} for the temperatures investigated in this study. Thus, analysis of the upper curves of unipolar or bipolar D–E loops resulted in nearly identical values of saturation and remnant polarizations $P_s(T)$ and $P_r(T)$ and relative permittivity $\varepsilon_r(T)$.

Moreover, the isothermal bipolar D–E loops corresponding to the ferroelectric phase plotted in figure 2 show the nonlinear behavior of the electric displacement D with respect to the electric field E. The electric displacement decreased sharply for a decreasing applied electric field around the critical electric field $E_{cr}(T)$. This nonlinearity was also observed for [110]-oriented PZN-4.5PT by Zhu *et al* [18] and was attributed to electric-field-induced phase transitions. The sudden decrease in electric displacement D around $E_{cr}(T)$ could also be explained by the 180° polarization switching in which the polarization of each crystal's unit cell reversed direction from $+P$ to $-P$ when the polarization vector aligned with the applied electric field vector [34, 37, 57]. Thus,

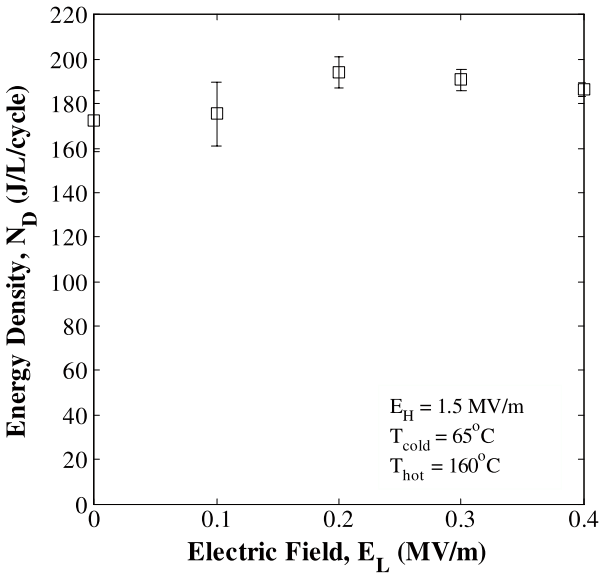

Figure 3. Energy density as a function of low electric field E_L varying from 0.0 to 0.4 MV m^{-1}. The high electric field was set as $E_H = 1.5$ MV m^{-1} while the cold and hot source temperatures were maintained at $T_{cold} = 65\,^{\circ}$C and $T_{hot} = 160\,^{\circ}$C, respectively.

the saturation polarization and relative permittivity varied nonlinearly as a function of electric field and the dielectric properties required in equation (4) were estimated from two piecewise regions of the isothermal bipolar *D–E* loops corresponding to the decreasing electric field branch. The electric displacement was assumed to depend linearly on the electric field in each region corresponding to electric field decreasing (i) from E_H to $E_{cr}(T)$ and (ii) from $E_{cr}(T)$ to E_L.

4.2. Effect of low electric field E_L

Figure 3 shows the average energy density harvested by sample 4 for five different Olsen cycles performed with low electric field E_L equal to 0.0, 0.1, 0.2, 0.3 and 0.4 MV m^{-1}. The high electric field was set as 1.5 MV m^{-1} while the cold and hot source temperatures were maintained at 65 and 160 °C, respectively. The error bars correspond to two standard deviations or 95% confidence interval. The energy density reached a maximum at $E_L = 0.2$ MV m^{-1}. In fact, the electric displacement vanished during process 4–1 for E_L set as 0.0 MV m^{-1} since this relaxor ferroelectric material possessed small remnant polarization at either temperatures used [58]. In other words, the sample was unable to retain its polarization at zero electric field. As a result, lowering the low electric field E_L from 0.2 to 0.0 MV m^{-1} resulted in a reduction in the energy density from 192 to 172 J l^{-1}/cycle. Meanwhile, raising the low electric field E_L from 0.2 to 0.4 MV m^{-1} reduced the energy density from 192 to 187 J l^{-1}/cycle, due to the reduced electric field span ($E_H - E_L$). Therefore, all measurements reported in the remainder of this study will correspond to $E_L = 0.2$ MV m^{-1}.

4.3. Sample variability

Figure 4 shows the energy density as a function of high electric field E_H between 0.4 and 1.5 MV m^{-1} collected from four different samples for temperatures T_{hot} equal to (a) 100 °C, (b) 110 °C, (c) 120 °C and (d) 130 °C. The low electric field E_L was 0.2 MV m^{-1} while the cold source temperature T_{cold} was maintained at 65 °C. The energy harvested represents the averaged values over five cycles performed under quasiequilibrium. Here also, the error bars represent a 95% confidence interval. Figure 4 indicates that sample variation was larger for low values of temperature T_{hot} and electric field E_H. In fact, the largest sample variation was found for $T_{hot} = 100\,^{\circ}$C and $E_H = 0.4$ MV m^{-1}, with a maximum relative difference among samples of 19.7%. Meanwhile, sample variability was the lowest for $T_{hot} = 130\,^{\circ}$C and $E_H = 1.5$ MV m^{-1}, with a maximum relative difference among samples of 9.1%. These results establish the consistency and repeatability of experimental measurements not only from one cycle to the next but also from one sample to the next.

4.4. Effect of cold source temperature T_{cold}

Figures 5 and 6 show the average energy density harvested by sample 4 as a function of high electric field E_H ranging from 0.4 to 2.5 MV m^{-1} for cold source temperature T_{cold} equal to 65 and 45 °C, respectively. Here also, the hot source temperature T_{hot} was equal to (a) 100 °C, (b) 120 °C, (c) 130 °C and (d) 160 °C. The low electric field was set as $E_L = 0.2$ MV m^{-1}. Figures 5 and 6 establish that the energy density N_D increased as the cold source temperature T_{cold} decreased. For example, for the conditions $E_H = 2.5$ MV m^{-1} and $T_{hot} = 160\,^{\circ}$C, the energy density increased from 343 to 442 J l^{-1}/cycle, or by 29% when T_{cold} was reduced from 65 to 45 °C. Indeed, this was attributed to the increase in electric displacement span $[D(E, T_{cold}) - D(E, T_{hot})]$. In other words, more free charges were collected at the electrode surface as T_{cold} was lowered. However, reducing T_{cold} from 65 to 45 °C increased the cycle period from 51.9 to 124 s and in turn decreased the corresponding power density from 6.61 to 3.56 W l^{-1}. This reduction in power density was attributed to an increase in the time required for isoelectric cooling (process 4–1) to be performed under quasiequilibrium conditions. This may be a consequence of the slow dielectric relaxation of PLZT in the ergodic relaxor phase at T_{cold} [58]. The dipole reorientation contributing to the polarization change slows down at low temperatures due to the increasing energy barrier necessary to activate and reorient the polar nanodomains [59].

4.5. Effect of hot source temperature T_{hot}

Figures 5 and 6 also establish that the energy density increased as the hot source temperature T_{hot} was raised from 100 to 160 °C for a given high electric field E_H. Between T_{cold} and $T_{hot} \geq T_{Curie}$, the 8/65/35 PLZT samples underwent a phase transition from ferroelectric (polar) to ergodic relaxor (non-polar). In fact, the largest energy density was obtained at T_{hot} near the ferroelectric–ergodic-relaxor phase transition temperatures $T_{Curie} \leq 160\,^{\circ}$C. However, increasing the operating temperature difference $(T_{hot} - T_{cold})$ in excess of 135 °C resulted in large thermal stresses, causing the sample to crack.

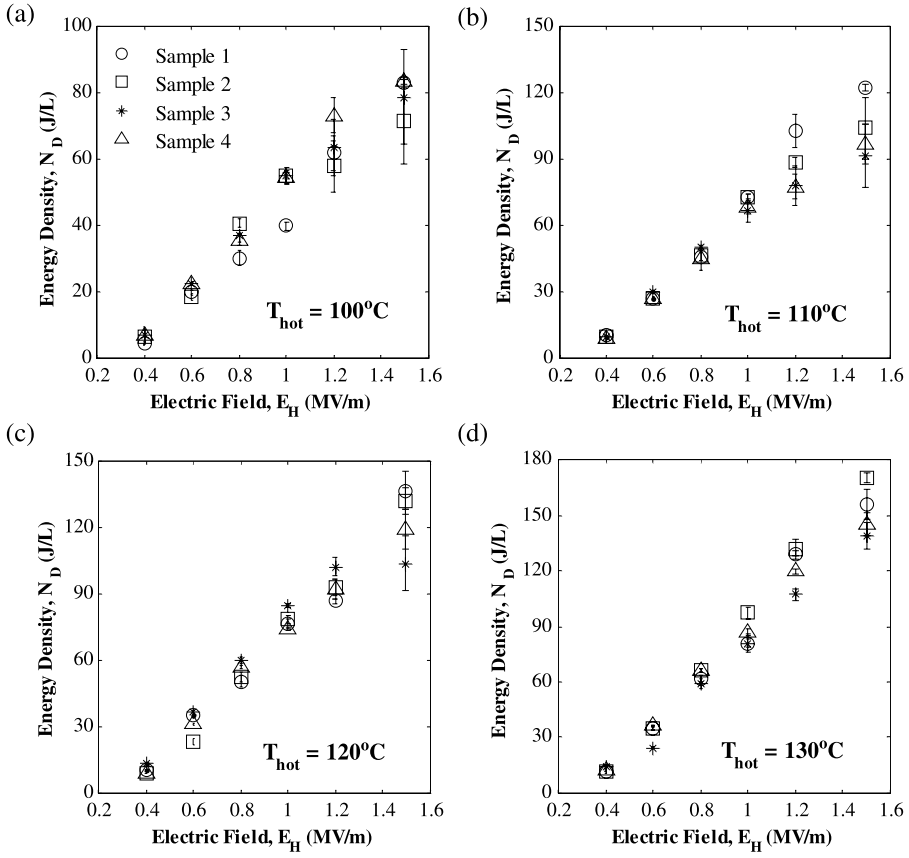

Figure 4. Experimentally measured energy density of 8/65/35 PLZT as a function of high electric field E_H for samples 1–4. The hot source temperature T_{hot} was equal to (a) 100 °C, (b) 110 °C, (c) 120 °C and (d) 130 °C. The high electric field E_H ranged from 0.4 to 1.5 MV m^{-1}. The cold source temperature T_{cold} and low electric field E_L were set as 65 °C and 0.2 MV m^{-1}, respectively. Sample variability was greatest at low temperatures and low electric fields.

4.6. Effect of high electric field E_H

Figures 5 and 6 indicate that, for a given hot source temperature T_{hot}, the energy density N_D increased as the high electric field E_H increased. Indeed, raising E_H increased the electric field span ($E_H - E_L$) resulting in larger energy densities as suggested by figure 1 and equation (4). However, the high electric field E_H was physically limited by the sample's dielectric strength, which was determined experimentally as 2.5 MV m^{-1} for samples with bare gold electrodes. We speculate that large strains were electrically induced within the samples when they were subject to cyclic high magnitude electrical loading, causing microcracks to develop along the domain boundaries [60]. In addition, electric field concentrations were formed such that the relative permittivity at the crack interior and the ceramic body were different, thus producing a strain [61, 62]. Ultimately, the propagation of these field-induced cracks led to sample failure [35]. Each sample used in this study cracked after ~200–300 Olsen cycles due to a combination of thermal stress and field-induced strains.

Two strategies were explored to increase the electrical breakdown field of 8/65/35 PLZT samples and maximize E_H. First, the specimen thickness was reduced from 650 μm (sample 4) to 370 μm (samples 5 and 6) and 290 μm (sample 7), since the electrical breakdown strength of ceramics was reported to increase with decreasing sample thickness [60]. This can be explained by the presence of fewer defects typically contained in thinner samples. Furthermore, a silicone conformal coating was applied to the PLZT samples 5–7 to reduce their susceptibility to cracking as suggested by [63]. Implementation of these strategies in sample 5 resulted in an increase of the material electrical breakdown from 2.5 to 4.5 MV m^{-1} for the operating conditions T_{cold} = 45 °C, T_{hot} = 160 °C and E_L = 0.2 MV m^{-1}. Then, the maximum energy density harvested per cycle increased by more than 50% from 442 J l^{-1} (sample 4) to 668 J l^{-1} (sample 5).

4.7. Maximum energy density

Figure 7 presents four consecutive Olsen cycles performed on sample 7 at 0.0178 Hz, corresponding to the maximum energy density achieved experimentally with this material. The cold and hot source temperatures were 25 and 160 °C while the electric field was cycled between E_L = 0.2 MV m^{-1} and E_H = 7.5 MV m^{-1}, respectively. An energy density of 887.5 ± 8.5 J l^{-1}/cycle was obtained, corresponding to a power density of 15.8 W l^{-1}.

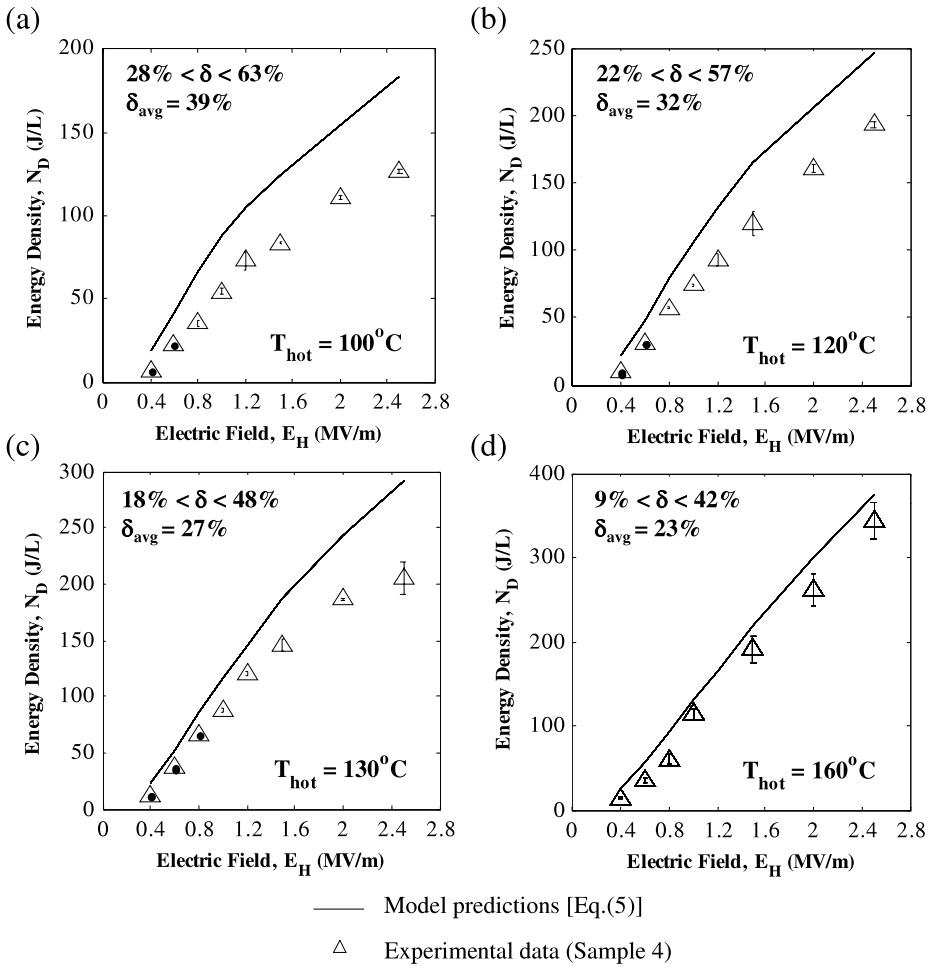

Figure 5. Experimentally measured energy density harvested by 8/65/35 PLZT (sample 4) as a function of high electric field. The hot source temperature T_{hot} was equal to (a) 100 °C, (b) 120 °C, (c) 130 °C and (d) 160 °C. The high electric field E_{H} ranged from 0.4 to 2.5 MV m^{-1}. The cold source temperature T_{cold} and low electric field E_{L} were set as 65 °C and 0.2 MV m^{-1}, respectively. The relative error between the model predictions and experimental data is denoted by δ.

Figure 7 shows that the *D*–*E* paths of the Olsen cycles were not closed since points 4 and 4′ did not coincide. The offset was caused by leakage current across the PLZT ceramic at high temperatures and/or large electric fields [10, 23, 64, 65]. The loss in energy density associated with the leakage current was estimated to be 15–20%. Moreover, note that the Olsen cycles did not follow a smooth path between E_{L} and E_{H} during isothermal processes 1–2 and 3–4 in the *D*–*E* diagram. It indicates that these processes were not performed under quasiequilibrium conditions [20]. This can be attributed to the inhomogeneity of the sample caused by the microcracks. Indeed, microcracks may have propagated along the grain boundaries of the sample while the Olsen cycle was performed under high electric fields and/or high temperatures [61]. These fractures introduced spatial variation in the local electric field near the crack front [62].

4.8. Discussion

The maximum energy density of 888 J l^{-1}/cycle produced by 8/65/35 PLZT should be compared with those achieved by other pyroelectric materials. In fact, table 2 compares the maximum energy density generated from the Olsen cycle for different materials, temperature ranges and operating electric fields. Note that a maximum energy density of 900 J l^{-1}/cycle using 60/40 P(VDF–TrFE) was reported by Olsen *et al* [4] for temperatures between 25 and 120 °C and electric fields cycled between 20 and 50 MV m^{-1}. However, it is unclear whether these experimental results were averaged over multiple cycles and if they were repeatable. In fact, Navid *et al* [23] produced 204 J l^{-1}/cycle averaged over five cycles for the same material, temperature range and operating electric fields. To the best of our knowledge, the maximum energy density reported in the present study for 8/65/35 PLZT is the largest energy density experimentally measured repeatably over multiple cycles. It could be further increased by increasing the electrical breakdown strength of the material. For example, samples can be (i) pre-stressed such as in a thin layer unimorph ferroelectric driver and sensor actuators to increase sample durability [66] or (ii) fabricated into single or multilayer thin film capacitors with thicknesses of the order of nanometers to increase the applied electric field without sample failure [67]. The use of thin film PLZT would substantially reduce the applied voltage delivered to the electrical circuit during the Olsen cycle. For example, only 7.5 V applied across a 10 μm thin PLZT film would be

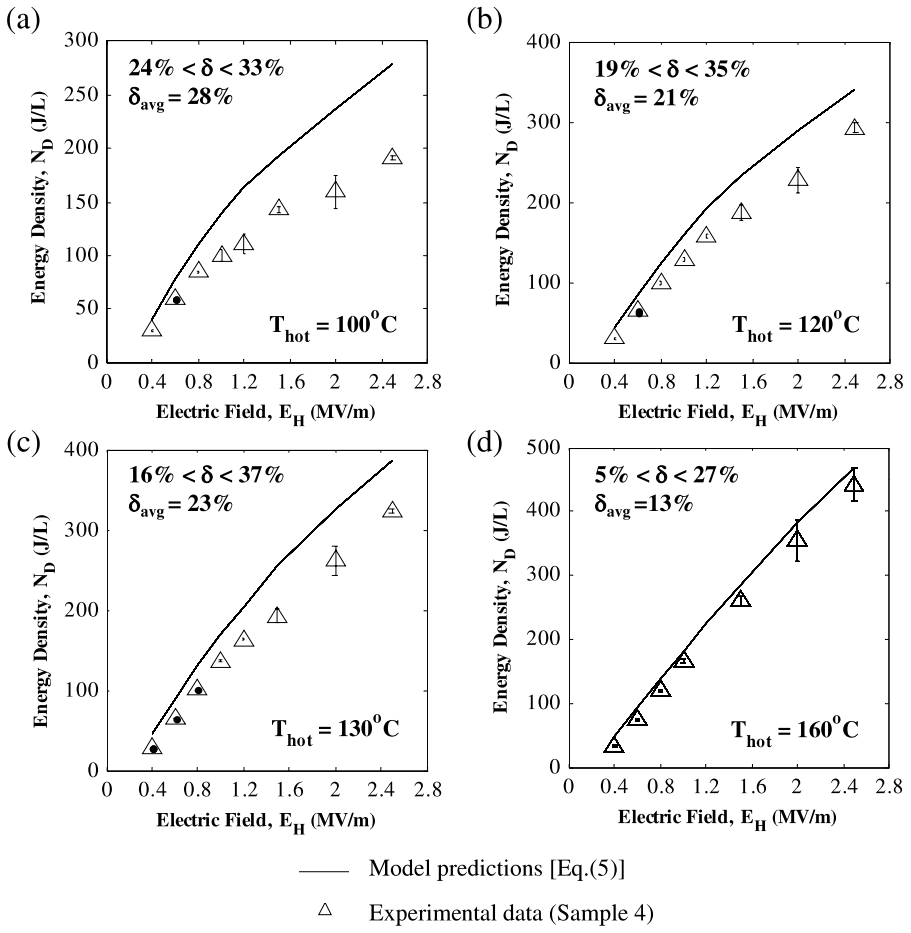

Figure 6. Experimentally measured energy density harvested by 8/65/35 PLZT (sample 4) as a function of high electric field. The hot source temperature T_{hot} was equal to (a) 100 °C, (b) 120 °C, (c) 130 °C and (d) 160 °C. The high electric field E_{H} ranged from 0.4 to 2.5 MV m^{-1}. The cold source temperature T_{cold} and low electric field E_{L} were set as 45 °C and 0.2 MV m^{-1}, respectively. The relative error between the model predictions and experimental data is denoted by δ.

Table 2. Comparison of maximum energy density achieved using the Olsen cycle or different materials, temperature ranges and operating electric fields.

Material	N_{D} (J l^{-1}/cycle)	T_{cold} (°C)	T_{hot} (°C)	E_{L} (MV m^{-1})	E_{H} (MV m^{-1})	Reference
PZST	131	157	177	0.4	3.2	[5]
PZST	130	145	178	1.2	3.2	[7]
PZST	100	146	159	0.0	2.9	[6]
PZST	0.4	110	170	0.0	2.8	[9]
73/27 P(VDF–TrFE)	30	23	67	23.0	53.0	[64]
60/40 P(VDF–TrFE)	52	58	77	4.1	47.2	[12]
60/40 P(VDF–TrFE)	130	67	81	20.3	37.9	[25]
60/40 P(VDF–TrFE)	521	25	110	20.0	50.0	[23]
60/40 P(VDF–TrFE)	900	25	120	20.0	60.0	[4]
61.3/29.7/9 P(VDF–TrFE–CFE)	50	0	25	0.0	25.0	[69]
PZN-4.5PT	217	100	160	0.0	2.0	[17]
PZN-5.5PT	150	100	190	0.0	1.2	[20]
PMN-10PT	186	30	80	0.0	3.5	[51]
PMN-32PT	100	80	170	0.0	0.9	[19]
8/65/35 PLZT	888	25	160	0.2	7.5	Present study

required to achieve an electric field of 7.5 MV m^{-1}instead of 2175 V required across a 290 μm thick sample (sample 7).

Moreover, the power output of devices using conduction [21], convection [25] or radiation [24] could be significantly improved by employing a multistaging technique [5]. This technique consists of placing pyroelectric materials in the order of increasing T_{Curie} between the cold and the hot source. The Curie temperature T_{Curie} of PLZT can be tuned by adjusting the lanthanum doping level (x) into PZT along with the Pb/Ti ratio. In fact, T_{Curie} was reported to be 65, 150,

Table 3. Critical electric field $E_{cr}(T)$, spontaneous polarization $P_s(T)$, remnant polarization $P_r(T)$ and relative permittivity $\epsilon_r(T)$ of 8/65/35 PLZT (sample 4) retrieved for two piecewise regions of isothermal bipolar *D–E* loops in the temperature range between 45 and 160 °C.

T (°C)	45	65	100	110	120	130	160
$E_{cr}(T)$ (MV m^{-1})	0.4	0.6	1.2	1.5	1.6	1.8	—
$E_H = 2.5$ MV m^{-1} to $E_{cr}(T)$							
$\epsilon_r(T)$	2624	3700	3977	3714	3700	3849	6439
$P_s(T)$ (C m^{-2})	0.265	0.220	0.155	0.151	0.139	0.118	0.0145
$E_{cr}(T)$ to $E_L = 0.2$ MV m^{-1}							
$\epsilon_r(T)$	10850	26050	15040	12547	11243	9651	6439
$P_r(T)$ (C m^{-2})	0.232	0.0856	0.0221	0.0188	0.0181	0.0148	0.0145

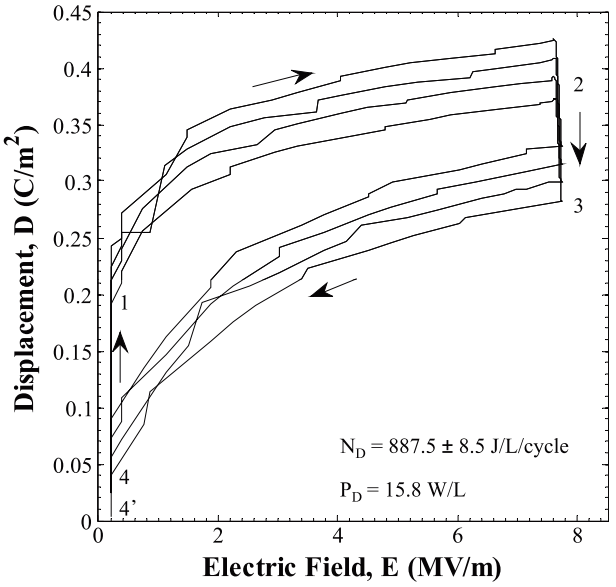

Figure 7. Electric displacement versus electric field diagram containing four experimental Olsen cycles (sample 7). The electric field was cycled between 0.2 and 7.5 MV m^{-1}. The cold source temperature T_{cold} and hot source temperature T_{hot} were 25 and 160 °C, respectively. The average energy density over four cycles was 887.5 J l^{-1} at 0.0178 Hz, corresponding to the largest energy harvested by 8/65/35 PLZT in this study.

240 and 320 °C in the absence of an electric field for the 65/35 Pb/Ti ratio and $x = 8$, 7, 6 and 2%, respectively [32].

5. Model predictions

As previously discussed, the electric displacement $D(E, T)$ of 8/65/35 PLZT varies nonlinearly when the electric field decreases from E_H to E_L. Therefore, the dielectric properties required in equation (4) were retrieved for two piecewise regions of the isothermal bipolar *D–E* loops corresponding to isothermal field reduction (i) from E_H to $E_{cr}(T)$ and (ii) from $E_{cr}(T)$ to E_L. The critical electric field $E_{cr}(T)$ was estimated from the inflection point in the isothermal *D–E* loop. It was found to increase with increasing temperature. Table 3 summarizes the critical field $E_{cr}(T)$, saturation and remnant polarizations $P_s(T)$ and $P_r(T)$, and relative permittivity $\varepsilon_r(T)$ of sample 4 for temperatures between 45 and 160 °C. The energy density predicted by the piecewise model can be expressed as the sum of two components:

$$N_D = N_D(E_L, E_{cr}, T_{cold}, T_{hot}) + N_D(E_{cr}, E_H, T_{cold}, T_{hot}) \quad (5)$$

where the function $N_D(E_{L/H}, E_{cr}, T_{cold}, T_{hot})$ is given by equation (4). The contribution from the region of decreasing electric field from E_H to $E_{cr}(T)$ can be predicted by equation (4) using the saturation polarization $P_s(T)$. The contribution from the region of decreasing electric field from $E_{cr}(T)$ to $E_L = 0.2$ MV m^{-1} can be predicted by equation (4) using the remnant polarization $P_r(T)$ instead of $P_s(T)$.

Figures 5 and 6 compare systematically the energy density obtained experimentally with predictions of equation (5) for four hot source temperatures $T_{hot} = 100$, 120, 130 and 160 °C and E_H ranging from 0.4 to 2.5 MV m^{-1}. The cold source temperature T_{cold} was set as 65 °C (figure 5) and 45 °C (figure 6). Note that the thermal expansion term $d_{33}x_3/s_{33}$ [31] corresponding to the secondary pyroelectric coefficient was ignored in the model predictions for PLZT. Indeed, Kandilian *et al* [19] observed that, for PMN-32PT, the Olsen cycle extended beyond the electric displacement bounded by the isothermal *D–E* loops. This was attributed to the contribution of thermal expansion to the energy density [19]. However, in the case of 8/65/35 PLZT, the Olsen cycles fell within the bounds of the isothermal *D–E* loops at both T_{cold} and T_{hot}. Therefore, the thermal expansion did not contribute to the energy density harvested. Similar observations were made for PZN-5.5PT [20].

Figures 5 and 6 also report the range and the average value of the relative error between experimental data and model predictions, denoted by δ and δ_{avg}, respectively. For example, the average relative error reached 39% and 28% for $T_{cold} = 65$ °C and $T_{cold} = 45$ °C at $T_{hot} = 100$ °C, respectively. For such a low value of $T_{hot} = 100$ °C, a small absolute difference in energy density resulted in a large relative error. However, the model predicted the experimental data reasonably well, for $T_{cold} = 45$ °C and $T_{hot} \geq 100$ °C and for $T_{cold} = 65$ °C and $T_{hot} \geq 130$ °C. In these cases, the average relative error between model predictions and experimental data was less than 30%.

Figure 8 shows the isothermal bipolar *D–E* loops collected on sample 4 at $T_{cold} = 45$ °C and T_{hot} equal to (a) 100 °C, (b) 120 °C, (c) 130 °C and (d) 160 °C overlaid

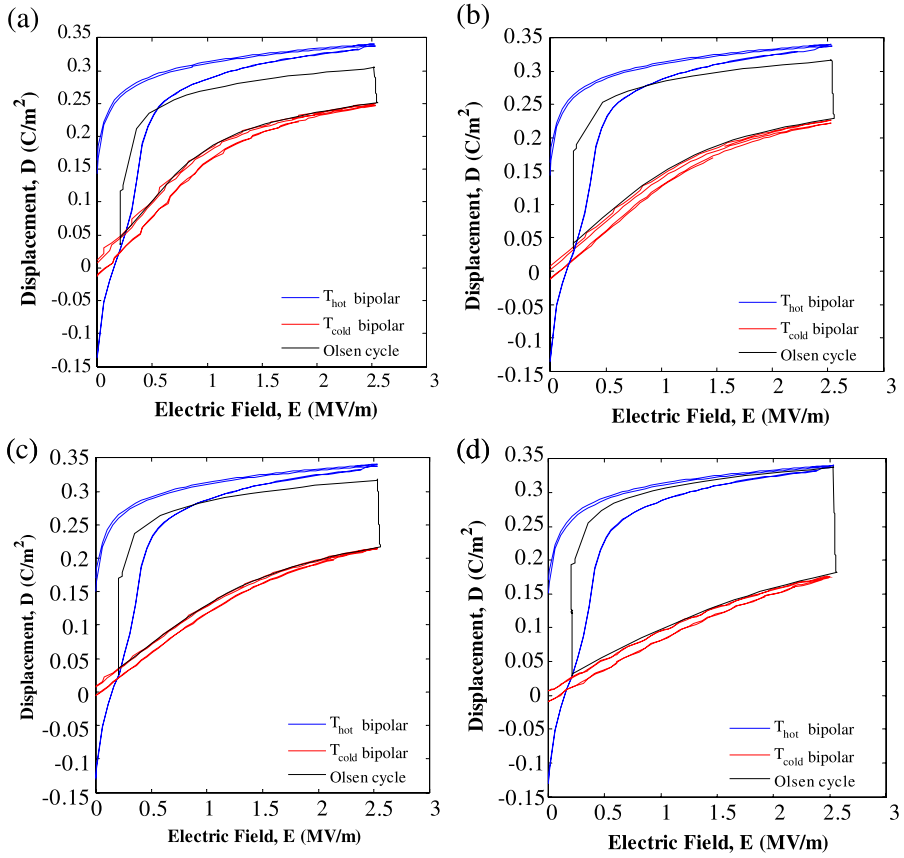

Figure 8. *D–E* diagram of isothermal bipolar *D–E* loops and experimental Olsen cycles for 8/65/35 PLZT (sample 4). The temperature T_{hot} was equal to (a) 100 °C, (b) 120 °C, (c) 130 °C and (d) 160 °C while $T_{\text{cold}} = 45$ °C, $E_{\text{L}} = 0.2$ MV m^{-1} and $E_{\text{H}} = 2.5$ MV m^{-1}. The Olsen cycle was vertically displaced to coincide with the *D–E* curve at T_{hot}.

with the corresponding Olsen cycles measured for $E_{\text{L}} = 0.2$ MV m^{-1} and $E_{\text{H}} = 2.5$ MV m^{-1}. Figure 8 illustrates the discrepancies between model predictions and experimental data. In fact, the Olsen cycles did not span the electric displacement between the isothermal bipolar *D–E* loops corresponding to T_{cold} and T_{hot}. It did not fully overlap either with the isothermal bipolar *D–E* loops at T_{cold} when the electric field increased from E_{L} to E_{H} (process 1–2). This may be attributed to a sudden increase in electric displacement associated with a field-induced phase transition [18] and/or possibly the existence of mixed phases [68] when the applied electric field increased from E_{L} to E_{cr} during the Olsen cycle. In contrast, this sharp increase in electric displacement was absent in the bipolar *D–E* loop at T_{cold}.

Overall, the model predictions were relatively good given the range of parameters explored, the simplicity of the model which did not account for leakage current and the complexity of the physical phenomena taking place during the Olsen cycle.

6. Conclusion

This paper reports, for the first time, experimental measurements of energy densities generated by ferroelectric relaxor 8/65/35 PLZT undergoing the Olsen cycle. A maximum energy density of 888 J l^{-1}/cycle corresponding to a power density of 15.8 W l^{-1} was obtained at 0.0178 Hz for operating temperatures between $T_{\text{cold}} = 25$ °C and $T_{\text{hot}} = 160$ °C and electric fields cycled between $E_{\text{L}} = 0.2$ MV m^{-1} and $E_{\text{H}} = 7.5$ MV m^{-1}. The maximum electric field and temperature swing were limited by electrical breakdown and thermal stress, respectively. Sample variability was relatively small, particularly at high temperatures and large electric fields. Moreover, increasing the operating temperature difference $T_{\text{hot}} - T_{\text{cold}}$ increased the energy density harvested but in turn reduced the power density produced due to an increase in the time required to perform isoelectric cooling and heating (processes 4–1 and 2–3) under quasiequilibrium conditions. Furthermore, the electrical breakdown strength and thus the energy and power densities of 8/65/35 PLZT increased as the sample thickness decreased. Finally, the experimental results confirmed the validity of the physical model [19] developed to predict energy densities of ferroelectric relaxors subjected to the Olsen cycle. Further experiments on the electric-field-induced phase transitions of 8/65/35 PLZT are necessary to better understand the behavior of the *D–E* loops and Olsen cycles obtained in this study.

Acknowledgments

FYL is grateful to the UCLA Mechanical and Aerospace Engineering Department for financial support in the form of

a Graduate Fellowship. IMM was supported in part by the NSF-IGERT program Clean Energy for Green Industry at UCLA.

References

[1] Lawrence Livermore National Laboratory *US Energy Flow Trends—2009* https://publicaffairs.llnl.gov/news/energy/energy.html#2009 September 16

[2] Taylor C F 1985 *The Internal Combustion Engine in Theory and Practice* (Cambridge, MA: MIT Press) chapter 8, Heat Losses

[3] Riffat S B and Ma X 2003 Thermoelectrics: a review of present and potential applications *Appl. Therm. Eng.* **23** 913–35

[4] Olsen R B and Bruno D A 1986 Pyroelectric conversion materials *Proc. 21st Intersociety Energy Conversion Engineering Conf. (Aug.)* (San Diego, CA: American Chemical Society) pp 89–93

[5] Olsen R B, Bruno D A and Briscoe J M 1984 Cascaded pyroelectric energy converter *Ferroelectrics* **59** 205–19

[6] Olsen R B, Bruno D A and Briscoe J M 1985 Pyroelectric conversion cycles *J. Appl. Phys.* **58** 4709–16

[7] Olsen R B, Bruno D A, Briscoe J M and Butler W F 1981 A pyroelectric energy converter which employs regeneration *Ferroelectrics* **38** 975–8

[8] Olsen R B 1982 Ferroelectric conversion of heat to electrical energy—a demonstration *J. Energy* **6** 91–5

[9] Olsen R B and Brown D D 1982 High-efficiency direct conversion of heat to electrical energy related pyroelectric measurements *Ferroelectrics* **40** 17–27

[10] Kouchachvili L and Ikura M 2008 Improving the efficiency of pyroelectric conversion *Int. J. Energy Res.* **32** 328–35

[11] Kouchachvili L and Ikura M 2006 High performance P(VDF-TrFE) copolymer for pyroelectric conversion *US Patent Specification* 7,323,506

[12] Ikura M 2002 Conversion of low-grade heat to electricity using pyroelectric copolymer *Ferroelectrics* **267** 403–8

[13] Navid A, Vanderpool D, Bah A and Pilon L 2010 Towards optimization of a pyroelectric energy converter for harvesting waste heat *Int. J. Heat Mass Transfer* **53** 4060–70

[14] Navid A, Lynch C S and Pilon L 2010 Purified and porous poly(vinylidene fluoride-trifluoroethylene) [P(VDF-TrFE)] thin films for pyroelectric infrared sensing and energy harvesting *Smart Mater. Struct.* **19** 055006

[15] Sebald G, Seveyrat L, Guyomar D, Lebrun L, Guiffard B and Pruvost S 2006 Electrocaloric and pyroelectric properties of $0.75Pb(Mg_{1/3}Nb_{2/3})O_3$–$0.25PbTiO_3$ single crystals *J. Appl. Phys.* **100** 124112

[16] Guyomar D, Pruvost S and Sebald G 2008 Energy harvesting based on FE–FE transition in ferroelectric single crystals *IEEE Trans. Ultrason. Ferroelectr. Freq. Control* **55** 279–85

[17] Khodayari A, Pruvost S, Sebald G, Guyomar D and Mohammadi S 2009 Nonlinear pyroelectric energy harvesting from relaxor single crystals *IEEE Trans. Ultrason. Ferroelectr. Freq. Control* **56** 693–9

[18] Zhu H, Pruvost S, Guyomar D and Khodayari A 2009 Thermal energy harvesting from $Pb(Zn_{1/3}Nb_{2/3})_{0.955}Ti_{0.045}O_3$ single crystals phase transitions *J. Appl. Phys.* **106** 124102

[19] Kandilian R, Navid A and Pilon L 2011 The pyroelectric energy harvesting capabilities of PMN-PT near the morphotropic phase boundary *Smart Mater. Struct.* **20** 055020

[20] McKinley I M, Kandilian R and Pilon L 2011 Waste heat energy harvesting using Olsen cycle on $0.945Pb(Zn_{1/3}Nb_{2/3})O_3$–$0.055PbTiO_3$ single crystals *Smart Mater. Struct.* in press

[21] Lee F, Navid A and Pilon L 2011 Pyroelectric waste heat energy harvesting using heat conduction *Appl. Therm. Eng.* in press

[22] Cuadras A, Gasulla M and Ferrari V 2010 Thermal energy harvesting through pyroelectricity *Sensors Actuators* A **158** 132–9

[23] Navid A and Pilon L 2011 Pyroelectric energy harvesting using Olsen cycles in purified and porous poly(vinylidene fluoride-trifuoroethylene) thin films *Smart Mater. Struct.* **20** 025012

[24] Fang J, Frederich H and Pilon L 2010 Harvesting nanoscale thermal radiation using pyroelectric materials *ASME J. Heat Transfer* **132** 092701

[25] Nguyen H, Navid A and Pilon L 2010 Pyroelectric energy converter using co-polymer P(VDF-TrFE) and the Olsen cycle cycle for waste heat energy harvesting *Appl. Therm. Eng.* **30** 2127–37

[26] Mane P, Xie J, Leang K and Mossi K 2011 Cyclic energy harvesting from pyroelectric materials *IEEE Trans. Ultrason. Ferroelectr. Freq. Control* **58** 10–7

[27] Hunter S, Lavrik N, Bannuru T, Mostafa S, Rajic S and Datskos P 2011 Development of MEMS based pyroelectric thermal energy harvesters *Energy Harvesting and Storage: Materials, Devices, and Applications II (Orlando, FL, April)* ed N Dhar, P Wijewarnasuriya and A Dutta, p 80350V

[28] Ravindran S K T, Huesgen T, Kroener M and Woias P 2011 A self-sustaining pyroelectric energy harvester utilizing spatial thermal gradients *Solid-State Sensors, Actuators and Microsystems Conf. (TRANSDUCERS), 2011 16th Int. (Beijing, June)* pp 657–60

[29] Lang S B 1974 *Sourcebook of Pyroelectricity* (New York, NY: Gordon and Breach, Science Publishers)

[30] Lang S B and Das-Gupta D K 2001 *Handbook of Advanced Electronic and Photonic Materials and Devices* vol 4 (San Diego, CA: Academic)

[31] Lines M E and Glass A M 1977 *Principles and Applications of Ferroelectrics and Related Materials* (Oxford: Clarendon)

[32] Haertling G H and Buchanan R C (ed) 1991 *Ceramic Materials for Electronics* (New York, NY: Dekker)

[33] Haertling G H 1999 Ferroelectric ceramics: history and technology *J. Am. Ceram. Soc.* **82** 797–818

[34] Lynch C S 1996 The effect of uniaxial stress on the electro-mechanical response of 8/65/35 PLZT *Acta Mater.* **44** 4137–9

[35] Liu T and Lynch C S 2006 Domain engineered relaxor ferroelectric single crystals *Contin. Mech. Thermodyn.* **18** 119–35

[36] Lynch C S 2011 Large field electromechanical measurement techniques for ferroelectric materials *Integr. Ferroelectr.* **111** 59–67

[37] Rauls M, Dong W, Huber J and Lynch C S 2011 The effect of temperature on the large field electromechanical response of relaxor ferroelectric 8/65/35 PLZT *Acta Mater.* **59** 2713–22

[38] Kamba S, Bovton V, Petzelt J, Rychetsky I, Mizaras R, Brilingas A, Banys J, Gringas J and Kosec M 2000 Dielectric dispersion of the relaxor PLZT ceramics in the frequency range 20 Hz–100 THz *J. Phys.: Condens. Matter* **12** 497519

[39] Bokov A A and Ye Z G 2006 Recent progress in relaxor ferroelectrics with perovskite structure *J. Mater. Sci.* **41** 31–52

[40] Vodopivec B, Filipič C, Levstik A, Holc J and Kutnjak Z 2004 Dielectric properties of partially disordered lanthanum-modified lead zirconate titanate relaxor ferroelectrics *Phys. Rev.* B **69** 224208

[41] Kalinin S V, Rodriguez B J, Budai J D, Jesse S, Morozovska A N, Bokov A A and Ye Z-G 2010 Direct evidence of mesoscopic dynamic heterogeneities at the surfaces of ergodic ferroelectric relaxors *Phys. Rev.* B **81** 064107

[42] Kholkin A 2010 Piezoresponse force microscopy of polarization dynamics in ferroelectrics *8th Int. Tutorial Workshop on Piezoresponse Force Microscopy and Nanoscale Electromechanics of Polar Materials* University of Science and Technology Beijing, Beijing
[43] Vodopivec B, Filipič C, Levstik A, Holc J and Kutnjak Z 2004 E-T phase diagram of the 6.5/65/35 PLZT incipient ferroelectric *J. Eur. Ceram. Soc.* **24** 1561–4
[44] Dellis J L, El Marssi M, Tilloloy P, Farhi R and Viehland D 1997 A dielectric study of the X/65/35 lanthanum-modified lead zirconate titanate series *Ferroelectrics* **201** 167–74
[45] Xi Y, Zhili C and Cross L E 1983 Polarization and depolarization behavior of hot pressed lead lanthanum zirconate titanate ceramics *J. Appl. Phys.* **54** 3399–403
[46] Divya A S and Kumar V 2009 A novel mechanism for relaxor-ferroelectric transition in PLZT (8/65/35) *J. Am. Ceram. Soc.* **92** 2029–32
[47] Kutnjak Z, Filipič C, Pirc R and Levstik A 1999 Slow dynamics and ergodicity breaking in a lanthanum-modified lead zirconate titanate relaxor system *Phys. Rev.* B **59** 294–301
[48] Bobnar V, Kutnjak Z, Pirc R and Levstik A 1999 Electric-field-temperature phase diagram of the relaxor ferroelectric lanthanum-modified lead zirconate titanate *Phys. Rev.* B **60** 6420–7
[49] Lang S B 2005 Pyroelectricity: from ancient curiosity to modern imaging tool *Phys. Today* **58** 31–6
[50] Lu S G *et al* 2010 Organic and inorganic relaxor ferroelectrics with giant electrocaloric effect *Appl. Phys. Lett.* **97** 162904
[51] Sebald G, Pruvost S and Guyomar D 2008 Energy harvesting based on Ericsson pyroelectric cycles in a relaxor ferroelectric ceramic *Smart Mater. Struct.* **17** 1–6
[52] Li Z, Xi Z, Xu Z and Yao X 2002 Dielectric/ferroelectric response and phase transition of PMN-0.32PT single crystal *J. Mater. Sci. Lett.* **21** 1325–7
[53] Incropera F P, DeWitt D P, Bergman T and Lavine A 2006 *Fundamentals of Heat and Mass Transfer* 6th edn (New York, NY: Wiley)
[54] Santos I A, Endo C, Zanin A L, Lente M H, Eiras J A and Garcia D 2001 Hot-pressed transparent PLZT ceramics from low cost chemical processing *Mater. Res.* **4** 291–5
[55] Simhony M, Bass M, Van Stryland E, Tenescu E and Levy B 1979 Fast response of PLZT pyroelectric detectors to megawatt CO_2 laser pulses *IEEE J. Quantum Electron.* **15** 206–8
[56] Liščić B 2009 Heat transfer control during quenching *Mater. Manuf. Processes* **24** 879–86
[57] Zhang L X, Ren X, Wang Y, Ke X Q, Ding X D and Sun J 2008 Novel electro-strain-effect in La-doped Pb(Zr, Ti)O_3 relaxor ferroelectrics *Int. Conf. on Martensitic Transformations (Santa Fe, NM, June–July)*
[58] Samara G A 2001 Ferroelectricity revisited—advances in materials and physics *Solid State Physics* vol 56 (San Diego, CA: Academic) pp 239–458
[59] Burkhanov A I and Shil'Nikov A V 2010 Super slow polarization relaxation in PLZT relaxor ceramics *Ferroelectrics* **299** 153–6
[60] Furman E and Cross L E 1994 Dielectric breakdown in PLZT 9.5/65/35 ceramics *Proc. 9th IEEE Int. Symp. on Ferroelectrics (Pennsylvania State University, College Park, PA, Aug.)* pp 577–80
[61] Lynch C S 1997 Fracture of ferroelectric and relaxor electro-ceramics: influence of electric field *Acta Mater.* **46** 599–608
[62] Cao H and Evans A G 1994 Electric-field-induced fatigue crack growth in piezoelectrics *J. Am. Ceram. Soc.* **77** 1783–6
[63] Kumar P, Sharma S, Thakur O P, Prakash C and Goel T C 2004 Dielectric, piezoelectric and pyroelectric properties of PMN-PT (68:32) system *Ceram. Int.* **30** 585–9
[64] Olsen R B, Bruno D A and Briscoe J M 1985 Pyroelectric conversion cycle of vinylidene fluoride-trifluoroethylene copolymer *J. Appl. Phys.* **57** 5036–42
[65] Yu J and Ikura M 2004 Direct conversion of low-grade heat to electricity using pyrorelectric conversion *Proc. 4th IASTED Int. Conf. European Power and Energy Systems (Rhodes)* pp 442–6
[66] Webber K G, Hopkinson D P and Lynch C S 2006 Application of a classical lamination theory model to the design of piezoelectric composite unimorph actuators *J. Intell. Mater. Syst. Struct.* **17** 29–34
[67] Dausch D E and Haertling G H 1996 The domain switching and structural characteristics of PLZT bulk ceramics and thin films chemically prepared from the same acetate precursor solutions *J. Mater. Sci.* **31** 3409–17
[68] Safari A, Panda R K and Janas V F 2011 Ferroelectric ceramics: processing, properties and applications www.rci.rutgers.edu/ ecerg/projects/ferroelectric.html
[69] Zhu H, Pruvost S, Cottinet P J and Guyomar D 2011 Energy harvesting by nonlinear capacitance variation for a relaxor ferroelectric poly(vinylidene fluoride-trifluoroethylene-chlorofluoroethylene) terpolymer *Appl. Phys. Lett.* **98** 222901